Available online at www.sciencedirect.com
ScienceDirect
Trans. Nonferrous Met. Soc. China 32(2022) 2290−2308
Transactions of Nonferrous Metals Society of China
www.tnmsc.cn

Microstructure evolution, mechanical properties and tailoring of coefficient of thermal expansion for Cu/Mo/Cu clad sheets fabricated by hot rolling

Jiang-jiang LIU, Ze-jun CHEN, Zhan-song ZHOU, Tai-qian MO, Peng-ju WANG, Wei-jun HE

Joint International Research Laboratory for Light Alloys, Ministry of Education, College of Materials Science and Engineering, Chongqing University, Chongqing 400044, China

Received 10 July 2021; accepted 17 February 2022

Abstract: The law of microstructure evolution and mechanical properties of hot roll bonded Cu/Mo/Cu clad sheets were systematically investigated and the theoretical prediction model of the coefficient of thermal expansion (CTE) of Cu/Mo/Cu clad sheets was established successfully. The results show that the deformation of Cu and Mo layers was gradually coherent with an increase in rolling reduction and temperature and excellent interface bonding was achieved under the condition of a large rolling reduction. The development of the microstructure and texture through the thickness of Cu and Mo layers was inhomogeneous. This phenomenon can be attributed to the friction between the roller and sheet surface and the uncoordinated deformation between Cu and Mo. The tensile strength of the clad sheets increased with increasing rolling reduction and the elongation was gradually decreased. The CTE of Cu/Mo/Cu clad sheets was related to the volume fraction of Mo. The finite element method can simulate the deformation and stress distribution during the thermal expansion process. The simulation result indicates that the terminal face of the clad sheets was sunken inward.

Key words: Cu/Mo/Cu clad sheets; roll bonding; collaborative deformation; mechanical properties; coefficient of thermal expansion; prediction model

1 Introduction

The growing requirement for enhanced properties continues to inspire us to develop novel materials. In recent years, clad sheets have generally been designed to meet practical requirements [1,2]. Cu/Mo/Cu clad sheets can be used in many fields due to their outstanding mechanical properties and thermal properties such as high strength, high thermal conductivity (TC) and low coefficient of thermal expansion (CTE) [3,4]. The TC and CTE of Cu/Mo/Cu clad sheets can be adjusted by changing the volume fraction of Mo [5]. It can be widely used as electronic packaging substrates and heat sink plates in microelectronic devices [6,7]. Some researchers have prepared Cu/Mo clad plates through various methods, such as explosion bonding [8], roll bonding [9], diffusion bonding [10] and diffusion-rolling bonding [11].

Roll bonding is one of the most common methods for preparing metal composite plates and can be widely used in the practical industrial production. This method has many advantages, such as high efficiency and low cost. Many multilayered composites have been successfully produced by roll bonding, such as Cu/Al [12,13], Mg/Al [14], Al/Ti [15], Al/Mg/Ti [16] and Al/Cu/Mg [17,18]. Both Cu and Mo have extremely different melting points (1084 and 2620 °C, respectively) and

Corresponding author: Ze-jun CHEN, Tel: +86-23-65123550, E-mail: zjchen@cqu.edu.cn
DOI: 10.1016/S1003-6326(22)65948-X

coefficients of thermal expansion (17.5×10^{-6} and $5.3\times10^{-6}\,K^{-1}$, respectively), so roll bonding between Cu and Mo is difficult. The roll bonding of metal materials is influenced by various factors, especially rolling reduction and temperature. A larger rolling reduction contributes to sound bonding [19]. For example, the interfacial bonding strength of carbon steel/stainless steel plates gradually increased with increasing rolling reduction [20]. In recent years, research on Cu/Mo clad sheets has mostly been focused on the bonding process and interface microstructure. YANG et al [11] fabricated the Mo−Cu composites by diffusion-rolling process and established atom-to-atom bonding between two metals. WANG et al [4] explored the Cu/Mo interface by multi-pass rolling and annealing cycle processes and achieved straight and coherent interface and strong interfacial strength. However, the effect of the rolling process on the microstructure evolution and properties of the Cu/Mo plates is not sufficient. In addition, for Cu/Mo/Cu electronic packaging materials, the thermal expansion property is very important. Based on previous studies [21], the CTE of Cu/Mo/Cu can be adjusted by achieving different thicknesses of the component metals. This provides the possibility to predict the CTE of the clad sheets before fabrication. Some researchers have deduced the theoretical calculation model for the CTE of composite materials. However, these models are usually not applicable to laminated composite plates, owing to the uneven deformation and stress of each part in the clad sheets. Turner's model [22] is based on the fact that only uniform hydrostatic stress exists in the phases. Kerner's model [23] accounts for both the shear and isostatic stresses developed in the component phases. Schapery's model [24] predicts the CTE of unidirectionally reinforced fiber composites. Finite element simulation can show the deformation mechanism of clad sheets under the effect of thermal loading well. It can be considered to correct the existing model by analyzing the inhomogeneity of deformation to gain a more precise theoretical calculation model to predict the CTE of Cu/Mo/Cu clad sheets.

In the present work, Cu/Mo/Cu clad sheets were fabricated by hot roll bonding. The microstructural evolution and the corresponding deformation mechanisms of clad sheets were investigated. The study mainly focuses on the effect of microstructure and layer thickness ratio on the mechanical properties and thermal-expansion property. Additionally, a theoretical calculation model for the CTE of Cu/Mo/Cu clad sheets was established, which provides a basis to predict the CTE of Cu/Mo/Cu clad sheets under different layer thickness ratios.

2 Experimental

2.1 Raw materials

The materials used in this research were pure Cu sheets with a thickness of 1.5 mm and pure Mo sheets with a thickness of 1.0 mm. The chemical compositions of the two materials are listed in Tables 1 and 2. The dimensions of the length and width of Cu and Mo sheet were 66 mm and 24 mm, respectively. The microstructure and texture of the raw materials are shown in Fig. 1. Clearly, Cu contained fine equiaxed grains with weak texture and Mo showed many elongated grains with strong texture.

Table 1 Chemical composition of pure Cu (wt.%)

Fe	Zn	O	P	S	Cu
0.05	0.04	0.004	0.003	0.006	Bal.

Table 2 Chemical composition of pure Mo (wt.%)

Fe	Ni	C	O	N	Mo
0.03	0.06	0.02	0.005	0.001	Bal.

2.2 Roll bonding

As shown in Fig. 2, the pure Cu sheets and pure Mo sheets were roughened with 120 grit SiC paper and then ultrasonically cleaned in absolute ethyl alcohol. After the surface treatment, the sheets were stacked alternately by the assemblage of Cu/Mo/Cu to form a sandwich plate with a thickness of 4.0 mm. To avoid sliding on each other, the sandwich plate was riveted from the short side. A universal testing machine was used to preload to make the Cu/Mo interface closely join together to avoid the interface from being oxidized in the process of heating as far as possible.

The riveted sheets were respectively heated at 850, 900 and 950 °C for 15 min in a furnace with the Ar atmosphere, and then immediately rolled to different reductions with mill rolls of 170 mm in diameter at a rolling speed of 0.2 m/s. When the heating temperature was 850 °C, the single-pass

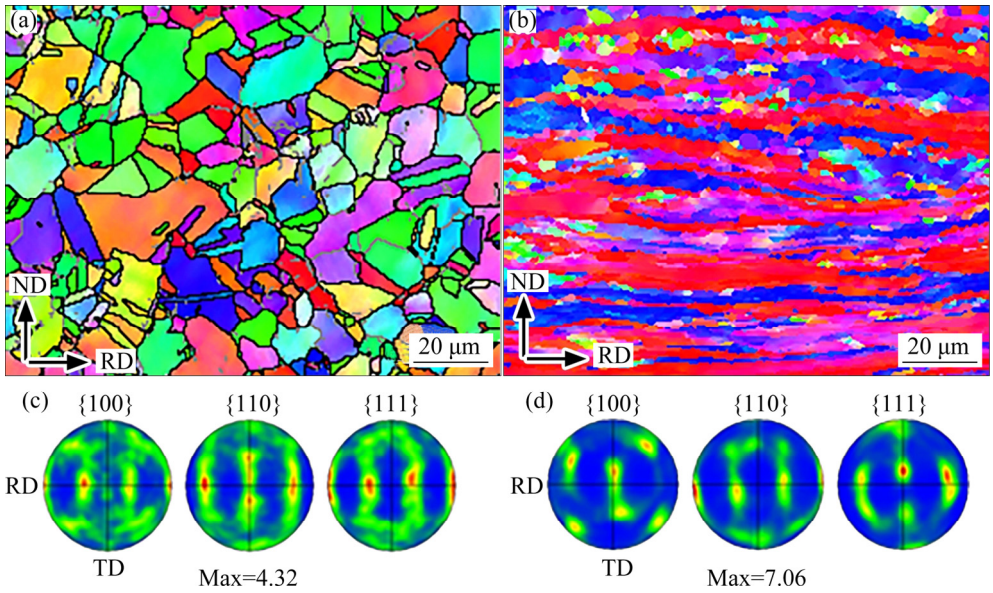

Fig. 1 Raw microstructure (a, b) and texture (c, d) of Cu (a, c) and Mo (b, d)

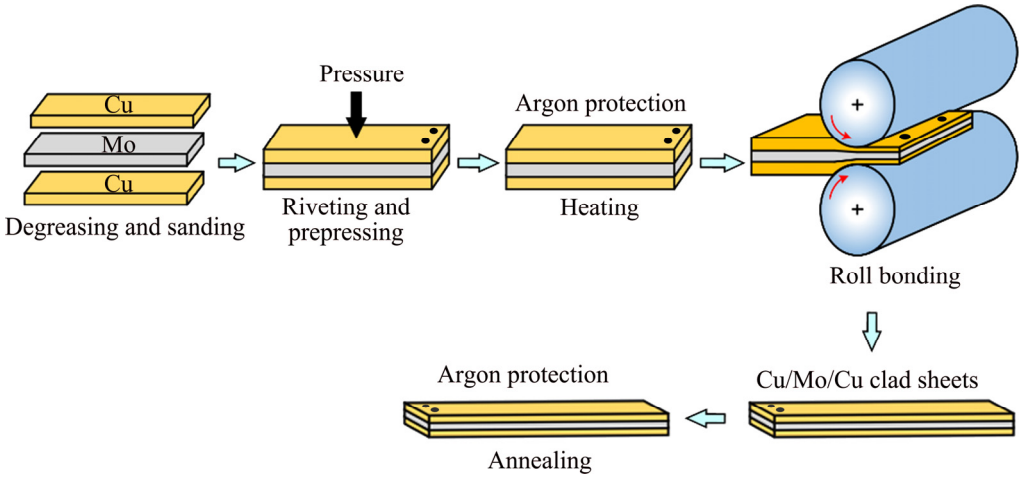

Fig. 2 Schematic diagram of fabrication process for hot roll bonded Cu/Mo/Cu clad sheets

reductions of approximately 0, 40%, 50%, 60% and 70% were conducted. As a comparison, a single-pass reduction of 70% was conducted when the heating temperatures were 900 and 950 °C.

The post-rolling annealing process was carried out under argon protection. The specimens with rolling temperatures of 850, 900 and 950 °C at a rolling reduction of 70% were annealed at 400 °C for 1 h to eliminate the internal stress and test the thermal expansion property of the clad sheets.

2.3 Investigation of structure and properties

The interface structure of Cu/Mo/Cu was characterized by field emission scanning electron microscope (SEM, JSM−7800F) equipped with an energy-dispersive spectroscopy (EDS) at a voltage of 20 kV. All micrographs were taken from the rolling direction (RD) and the normal direction (ND). The Cu layers for SEM were electropolished in a solution containing 10 mL phosphoric acid, 10 mL ethanol and 20 mL distilled water at a voltage of 8 V for 20 s. The Mo layer was electropolished in a solution containing 30 mL methanol, 1.5 mL perchloric acid and 18.5 mL 2-butoxy ethanol at a voltage of 20 V for 20 s. Electron backscatter diffraction (EBSD) measurements were carried out by a TESCAN MIRA3 scanning electron microscope with a system at 20 kV and a working distance of 15 mm. The diffraction data were obtained with a step size of 0.3 μm. The collected data were analyzed using the HKL® Channel 5 analysis software. The texture

of the Mo layer was detected by X-ray diffraction (XRD, Rigaku D/max 2500PC with Cu K_α radiation). The detection region was along the rolling plane with an area of 8 mm × 6 mm. The (110), (200), (211) and (222) peaks were fitted by Labo Tex 3.0 software.

The hardness through the thickness of clad sheets was examined by a Vickers hardness test at room temperature. Hardness measurements were carried out using a 50 g load with a dwell time of 10 s, and the average hardness from three independent measurements was calculated. A universal tensile test was used to determine both the tensile strength and the elongation of the clad sheets. The tensile speed was 1 mm/min. The tensile specimen was 15 mm in length and 4 mm in width. The tensile direction was parallel to the RD of the clad sheets. The CTE was measured by a thermal dilatometer (NETZSCH DIL 402 C). The measurement ranged from room temperature to 450 °C at a speed of 10 °C/min in a protected atmosphere of Ar. The specimen was 25 mm in length and 5 mm in width.

2.4 Finite element simulation

To better demonstrate the deformation and stress of Cu/Mo/Cu clad sheets under the effect of thermal loading, finite element analysis was carried out. According to the symmetrical characterization of Cu/Mo/Cu clad sheets, the 2D model was set up with the RD−ND plane and the model was meshed with a 2D quadrilateral element with four nodes. The Cu/Mo/Cu clad sheets were defined as three parts. The geometric dimensions and the setting of the thermal analysis conditions were the same as the practical specimens. The connection type of the Cu/Mo/Cu interface was bonded, which ensured neither normal nor tangential separation of each layer.

3 Results and discussion

3.1 Cu/Mo interface evolution of different rolling processes

Figure 3 presents the Cu/Mo interface microstructures at different rolling reductions and temperatures. A schematic diagram of the Cu/Mo interface is shown in Fig. 3(a). The interface microstructure and O element distribution of the unrolled specimen are shown in Figs. 3(a_1) and (a_2) respectively, and many continuous oxides can be observed at the Cu/Mo interface. It is not difficult to understand that Cu and Mo are easily oxidized at high temperatures, so many oxides will inevitably appear at the interface. In the rolled specimens, it can be observed that a relatively straight Cu/Mo interface changed into a wavy morphology with an increased rolling reduction when the temperature was 850 °C. A similar behavior of interface appeared in Al/Ti clad sheets [25]. When the rolling reduction is 50%, the oxide content is much lower than that of the unrolled plate and the interface is relatively straight. However, continuous oxides can still be seen at a higher magnification, as shown in Fig. 3(b_1). At the same time, the continuous O element distribution can be seen in Fig. 3(b_2). It must be pointed out that rolling reduction is lower, and continuous oxides are very difficult to break under smaller rolling force [26]. As the rolling reduction increased, the interface was bonded with a toothed shape with a rolling reduction of 60%, and the oxides at the interface started to break. A small quantity of oxides still existed in local areas, as shown in Fig. 3(c_1). When the rolling reduction further increased to 70%, Cu was inserted into Mo, and the oxides at the interface started to disappear, as presented in Fig. 3(d_1). This result demonstrates the uncoordinated deformation of the clad sheets due to the enormous mechanical difference between the Cu and Mo layers. The difference in the flow properties between the constituent layers led to shearing at the Cu/Mo interface, which resulted in the Mo layer embedded by the Cu layer. Similarly, this phenomenon was also reported in other roll bonded plates, such as Ti/steel [26] and Al/Cu [27].

When the rolling reduction was 70%, the Cu/Mo interface showed a wavy morphology at rolling temperatures of 900 and 950 °C. The oxides of the interface can hardly be seen, as presented in Figs. 3(e_1) and (f_1). This finding indicates that the sound interface is mainly attributed to larger rolling reductions, and the effect of temperature on the interface morphology is very small. Alternatively, rolling reduction has an important effect on the interface morphology. Regarding the evolution of interface structure, most previous investigations have focused on the effect of rolling reduction [15,26].

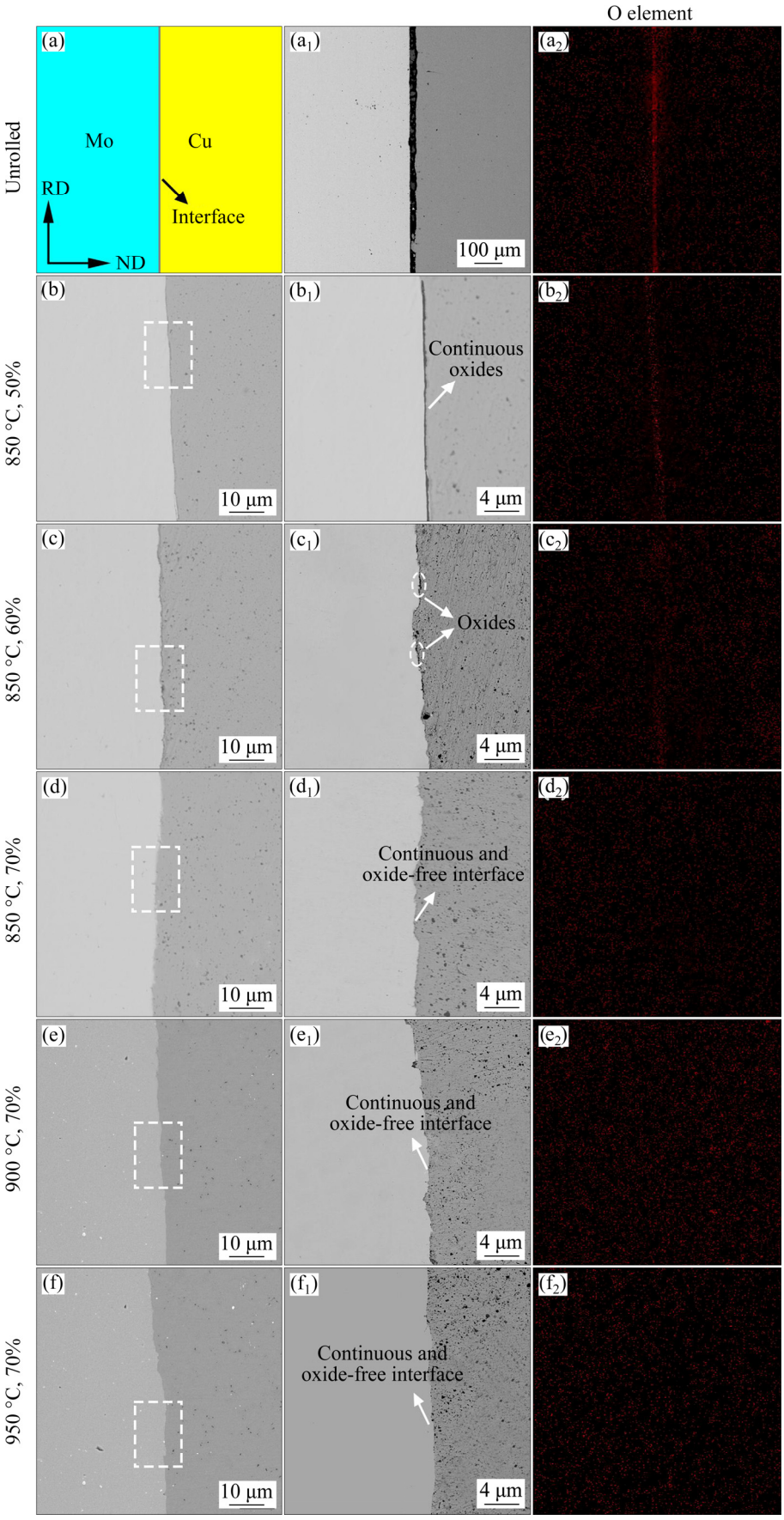

Fig. 3 Cu/Mo interface microstructures at different rolling reductions and temperatures

3.2 Variation in rolling reduction ratio of Mo to Cu layer

The rolling reduction (ε) of the Cu layer is different from the Mo layer during hot roll bonding because of the difference in mechanical properties between Cu and Mo. Table 3 lists the rolling reduction of Cu and Mo layers as well as their ratios at different rolling reductions and temperatures, which were measured on the RD−ND plane of the Cu/Mo/Cu clad sheets. The variations in the reduction ratio of the Mo to Cu layer with different rolling reductions and temperatures are shown in Figs. 4(a) and (b), respectively.

The $\varepsilon_{Cu}/\varepsilon_{Mo}$ ratio gradually increased (Fig. 4(a)), which indicated that the deformation difference between the two metals gradually decreased with increasing the rolling reduction. Moreover, the reduction of the Cu layer was closer to that of the clad sheets under a given rolling reduction based on Table 3. Notably, the deformation resistance of Cu is lower compared with Mo at higher temperatures. When the rolling reduction is lower, the Cu layer deforms easily with a smaller rolling force, while the deformation of the Mo layer is smaller. The deformation of the clad sheets is almost entirely undertaken by the Cu layer. When the rolling reduction is increased, the larger rolling force renders a toothed combination at the Cu/Mo interface, as shown in Fig. 3, and the pressure from the roller easily penetrates into the Mo layer, so that the deformation of Cu and Mo tends to be consistent [28].

When the rolling reduction is 70%, the deformation between the Cu and Mo layers tends to be more consistent with that at the elevated rolling temperatures (Fig. 4(b)). Figure 5 exhibits the inverse pore figures (IPFs) of the Mo plate at different annealing temperatures for approximately 15 min, which indicates the microstructure of the Mo sheet before entering the roller. When the rolling temperature is 900 °C, the deformation resistance of Mo is lower than that at 850 °C, but the softening degree of Cu has reached the limit. When the temperature reaches 950 °C, Mo presents obvious recrystallization behavior (Fig. 5(c)), which leads to a reduction in the deformation resistance. Therefore, Cu and Mo show good cooperative deformation under such a large rolling reduction. It can be confirmed that a large rolling reduction and high rolling temperature contribute to the collaborative deformation of Cu and Mo.

Table 3 Rolling reduction of Cu and Mo layers and their ratio at different rolling processes

Temperature/ °C	Total reduction/%	Thickness of Mo layer/mm	Reduction of Mo layer/%	Thickness of Cu layer/mm	Reduction of Cu layer/%	Reduction ratio of Mo to Cu layer
850	40	0.860	14.0	0.760	49.3	0.284
850	50	0.694	30.6	0.688	54.1	0.567
850	60	0.584	41.6	0.483	67.8	0.614
850	70	0.477	52.3	0.441	70.6	0.740
900	70	0.448	55.2	0.456	69.6	0.793
950	70	0.390	60.9	0.470	68.7	0.886

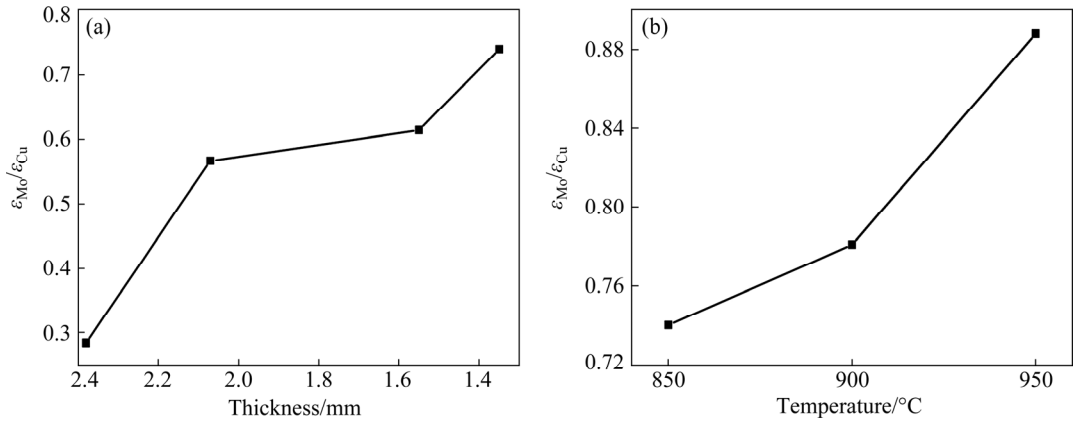

Fig. 4 Variation in reduction ratio of Mo to Cu layer at different rolling reductions (a) and rolling temperatures (b)

3.3 Microstructure evolution through thickness of Cu layer

Figure 6 shows the microstructure of the Cu layer of different regions in the Cu/Mo/Cu clad sheets fabricated by hot rolling under different rolling reductions. The heated microstructure of Cu is given in Fig. 6(a), and course equiaxed grains can be observed. It is not difficult to understand that 850 °C further exceeds the recrystallization temperature of Cu, and the growth speed of grains is very fast [29]. Low-angle grain boundaries (LAGBs) can hardly be seen in these grains, which is a complete recrystallization state. After the clad sheets were rolled, the grains were drastically refined.

When the rolling reduction is 50%, as shown in Fig. 6(b), the grain orientation of the Cu layer is random. However, it is obvious that the grain size of the middle zone is larger than that of the near-roller and near-interface zones. The microstructure through the thickness of Cu layer is inhomogeneous because the force states are different for different zones. The grains of middle zone are mainly affected by normal stress. The grains on near-roller and near-interface zones are also subjected to shear stress from the roller and Mo layer. The shear force from the roller and Mo layer can refine the grains. The phenomenon is similar to the process of friction stir welding [30] and equal-channel angle pressing [31], therefore, the grains of shear zone are obviously refined. To observe the grain boundaries more clearly, Fig. 7 shows the grain boundary distribution of different reductions, in which high-angle grain boundaries

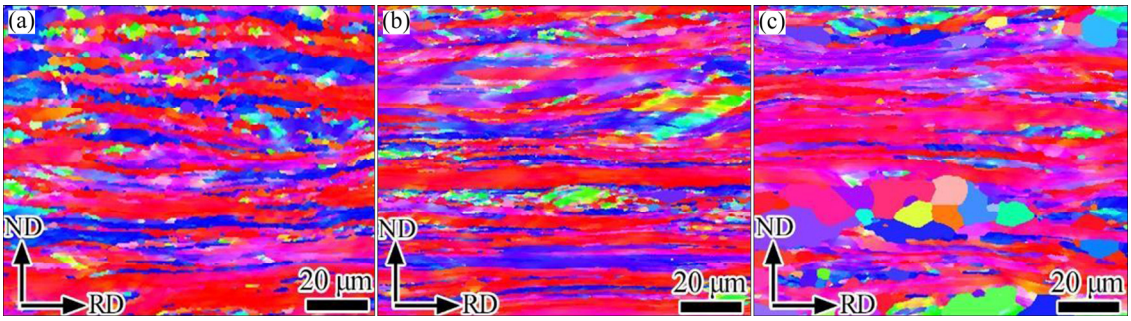

Fig. 5 IPFs of Mo plate at different annealing temperatures for about 15 min: (a) 850 °C; (b) 900 °C; (c) 950 °C

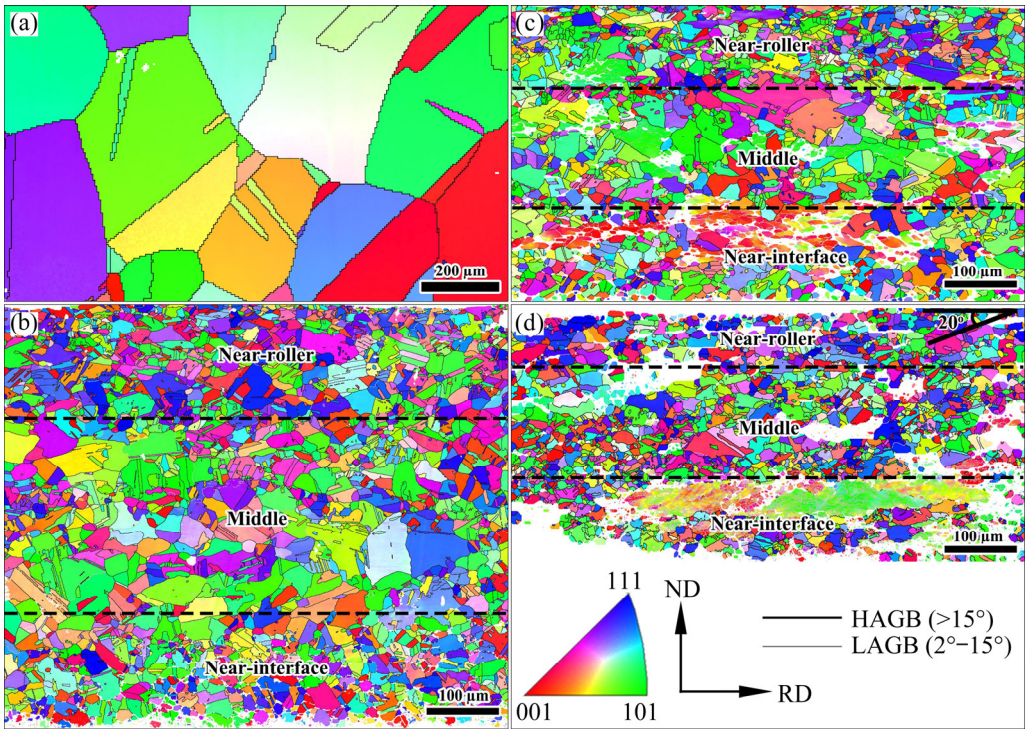

Fig. 6 IPFs of Cu layer under different rolling reductions at 850 °C: (a) 0; (b) 50%; (c) 60%; (d) 70%

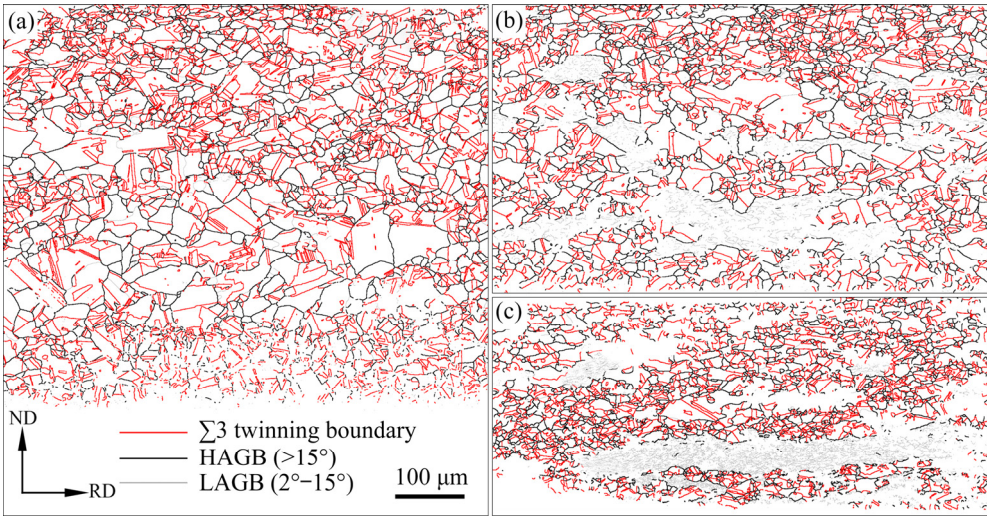

Fig. 7 Grain boundary distribution of Cu layer under different reductions at 850 °C: (a) 50%; (b) 60%; (c) 70%

(HAGBs) are presented by the black lines, low-angle grain boundaries (LAGBs) are presented by the gray lines and twin boundaries (TBs) are presented by the red lines. The specimen with a 50% reduction hardly exhibited LAGBs. This result indicated that the grains were almost recrystallized completely.

When the rolling reduction is 60%, as shown in Fig. 6(c), the overall grains are smaller than those of the 50% rolling reduction. Since the deformation degree of Cu increases with increasing rolling reduction of the clad sheets, the grains can be further broken under the larger rolling reduction. At the same time, the reduction of 60% has some LAGBs in the local zones (Fig. 7(b)), which is attributed to the incomplete recrystallization. The grains of the middle zone are larger than those of the near-roller and near-interface zones, which exhibits a similar phenomenon to the sample with a rolling reduction of 50%.

When the rolling reduction increases to 70%, as indicated in Fig. 6(d), the grains are the smallest in the three rolling reductions. The Cu layer experienced a larger deformation compared with the reduction of 60%. The grain sizes of different zones had no obvious differences. The shear effect from the roller can penetrate deeply into the nearby zone with increasing reduction. The grains of the middle zone can be fragmented under a larger rolling force and there are a lot of LAGBs in the local zones (Fig. 7(c)). Furthermore, the grains showed a certain banded distribution under the effect of the roller. The shear band was along the direction of approximately 20° to the RD, as shown in Fig. 6(d).

In general, the inhomogeneity of the microstructure through the thickness of the Cu layer can be attributed to the effect of the roll-gap geometry and the friction between the roller and sheet surface as well as the uncoordinated deformation between constituent layers [28]. The effect of the roll-gap geometry depends on the l/h ratio, where l represents the projected length of contact between the roller and the specimen, and h is the average thickness of the clad sheets [32]. When the l/h ratio is less than 0.5, the shear effect from the roller can be produced at the intermediate layer. When the l/h ratio is more than 5, the shear effect will disappear. In this experiment, the l/h ratios were 4.22, 5.20 and 5.59 for 50%, 60% and 70% reductions, respectively. This indicates that the inhomogeneous microstructure of the Cu layer may be affected by roll-gap geometry when the rolling reduction is 50%. With the increase in rolling reduction, the friction between the roller and Cu surface and the uncoordinated deformation between Cu and Mo layers are the main factors affecting the inhomogeneous microstructure.

Based on the above results, at a certain reduction, the average grain size in different zones of the Cu layer was distinct. The inhomogeneity of deformation through the thickness of the Cu layer can be attributed to the effect of friction from the roller and the uncoordinated deformation between constituent layers [26,28]. The rolling reduction had a significant effect on the deformation inhomogeneity through the Cu layer. A similar

phenomenon appeared in 6061/TC4/6061 rolled laminated composites [28] and the study indicated that the microstructure through the thickness of the Al layer was very inhomogeneous, and as the thickness direction moved from the near-roller side to the near-interface side of the Al layer, the grain size gradually decreased.

In Fig. 7, some LAGBs existed in local zones with 60% and 70% rolling reductions. The deformation of Cu increased with increasing rolling reduction, and the number of internal dislocations increased. In general, a high fraction of LAGBs is related to a high density of dislocations [33]. In this experiment, the rolling temperature was 850 °C, which far exceeds the recrystallization temperature of Cu. However, it is difficult to complete the recrystallization process with fast cooling speed after rolling. Especially at high rolling reductions with serious internal deformation, some LAGBs are preserved. Furthermore, so many fine recrystallized grains existed in the surroundings of the LAGBs (Fig. 7(c)). A larger rolling reduction led to more local deformation, which may promote the nucleation of fine recrystallized grains [26]. In addition, it is important to note that all recrystallized grains contain TBs. This indicates that the growth of Cu grains heavily depends on the twinning process, and the occurrence of twinning contributes to the recrystallization process [34].

The histograms of the misorientation angle of the Cu layer under different rolling reductions are shown in Fig. 8. The average misorientation is gradually decreased with the increase of rolling reduction. When the rolling reduction changes from 50% to 60%, the average misorientation angle changes from 44.08° to 29.83°. This change can be attributed to the increase in the LAGBs amount. The HAGBs are mainly concentrated at a peak angle of 60°, which represents Σ3 boundaries (TBs), characterized by a 60° rotation with respect to ⟨111⟩. The secondary peak of the HAGBs is near 40°, which represents Σ9 boundaries, characterized by a 38.94° rotation with respect to ⟨110⟩. They are the common grain boundary types in the recrystallization process of Cu [34,35].

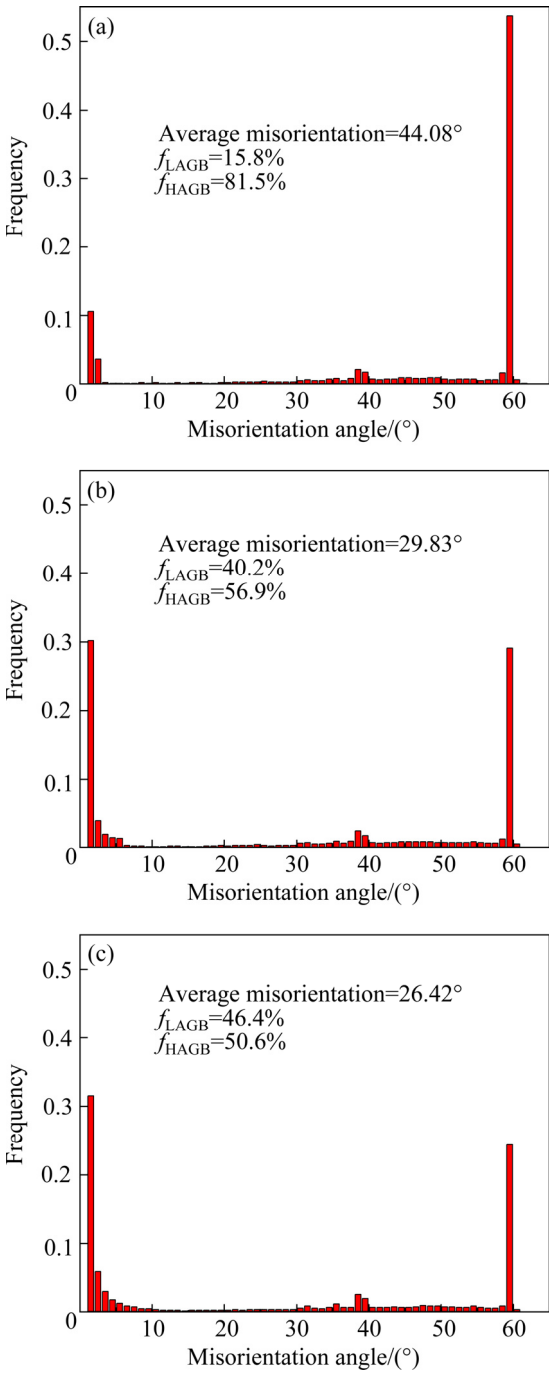

Fig. 8 Distribution of misorientation angles of Cu layer at 850 °C: (a) 50%; (b) 60%; (c) 70%

3.4 Texture evolution through thickness of Mo layer

Figure 9 shows the IPFs of the Mo layer in the near-interface and middle zones at different rolling reductions. It is obvious that almost all grains are elongated fibers. There is a little of unrecognized area of near-interface zone in the IPFs due to the larger stress from the Cu layer. The texture components are mainly composed of the {100}⟨*uvw*⟩ and {111}⟨*uvw*⟩ textures (as displayed by arrows in Fig. 9(b)), which is the same as the roll texture of other refractory metals of the body-centered cube (bcc) structure, such as W [36] and

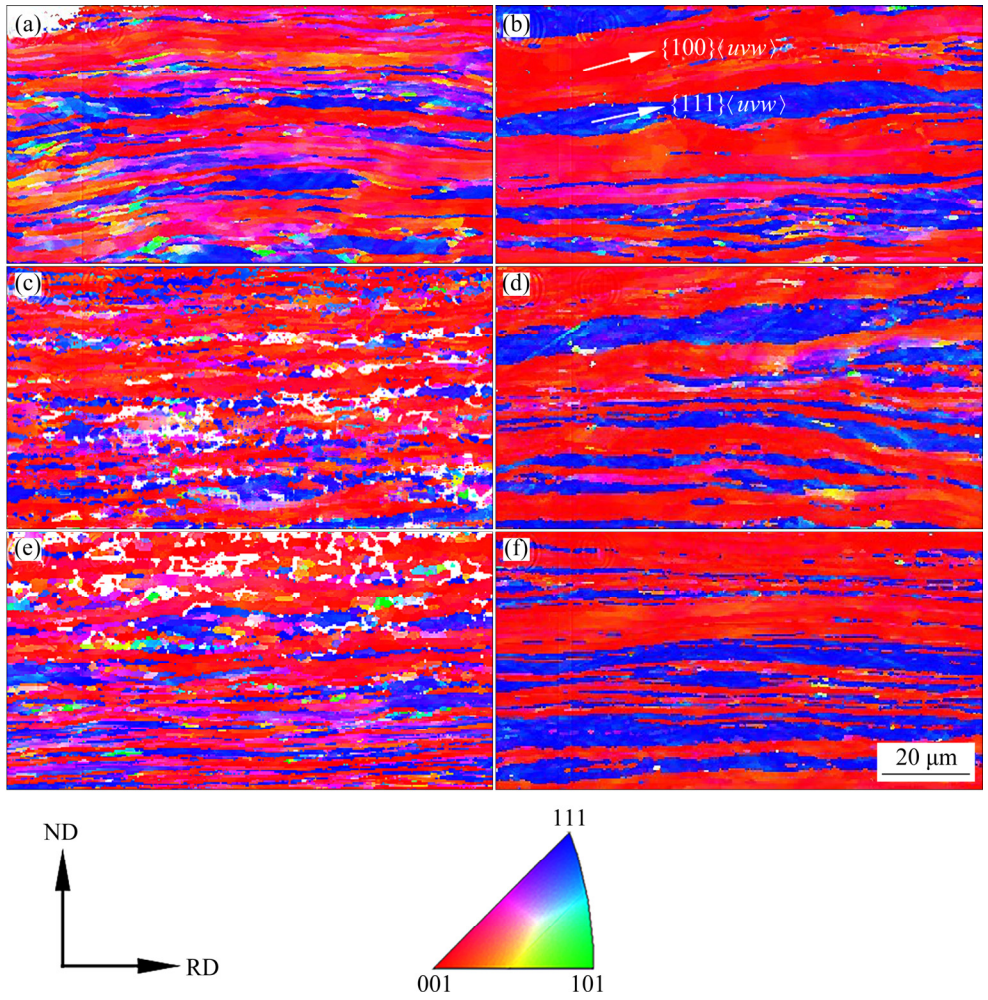

Fig. 9 IPFs of Mo layer in near-interface and middle zones at rolling temperature of 850 °C: (a) Near-interface, 50%; (b) Middle, 50%; (c) Near-interface, 60%; (d) Middle, 60%; (e) Near-interface, 70%; (f) Middle, 70%

Ta [37]. Recently, DENG [38] reported that the cold-rolled Ta plate mainly contains the {111}⟨*uvw*⟩ and {100}⟨*uvw*⟩ textures.

Figure 10 shows the pore figures (PFs) obtained by XRD. The {200} and {222} line profiles are the second-order diffractions of the {100} and {111} grains, respectively. Compared with the near-interface zone, the pole intensity of the middle zone was larger. The pole intensity increased with increasing rolling reduction.

Figure 11 shows the fraction of several textures in different zones of the Mo layer. The four textures of {001}⟨110⟩, {112}⟨110⟩, {111}⟨112⟩ and {111}⟨110⟩ were counted and analyzed. In the middle zone, as the rolling reduction increased, the {100}⟨110⟩ texture was strengthened, whereas the {111}⟨*uvw*⟩ texture was weakened. It can be explained that the {111}⟨*uvw*⟩ changed to {100}⟨110⟩ under the larger rolling reduction. According to previous reports [39,40], the {111}⟨*uvw*⟩ texture is unstable, but the {100} orientation grain shows excellent stability. YOU [41] found that Mo plates formed α-fiber textures with a cold rolling reduction of 30%−60% and γ-fiber textures with reduction of 70%−80%. The deformation degree of the Mo layer gradually increases with increasing rolling reduction. The {112}⟨110⟩ texture was tiny in the middle zone and was not discussed. For a given rolling reduction, there are more {112}⟨110⟩ textures in the near-interface region than that of the middle zone. The Mo layer is subjected to significant shear stress from the Cu layer due to collaborative deformation. Shear stress makes bcc metals easily form {112}⟨110⟩ texture and weakens the {111}⟨*uvw*⟩ and {100}⟨*uvw*⟩ textures [42]. The rotating cubic texture {001}⟨110⟩ and γ-fiber texture ({111}⟨112⟩ and {111}⟨110⟩) in the middle zone are significantly higher than the region near the interface.

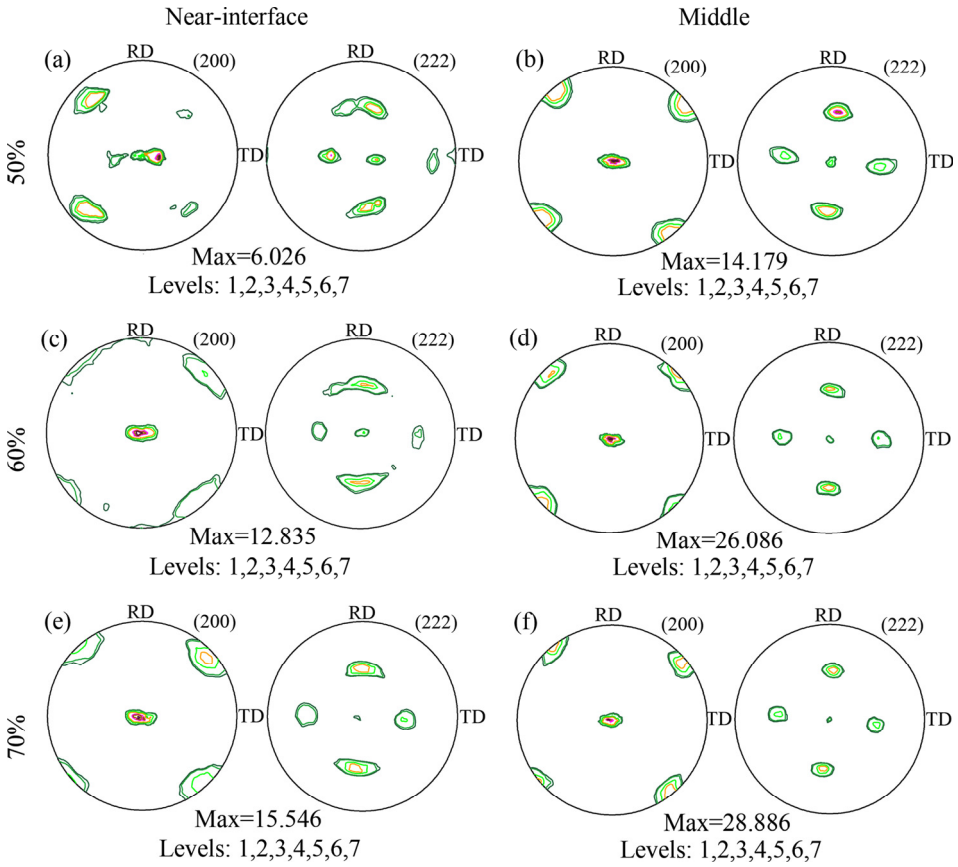

Fig. 10 PFs of Mo layer in near-interface and middle zones at rolling temperature of 850 °C

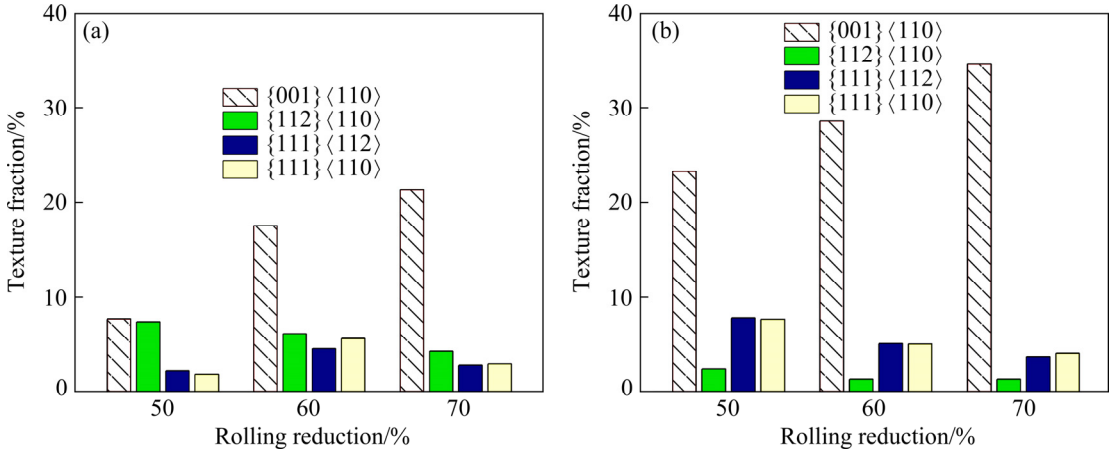

Fig. 11 Fractions of textures in different zones of Mo layer at rolling temperature of 850 °C: (a) Near-interface zone; (b) Middle zone

3.5 Mechanical properties of Cu/Mo/Cu clad sheets

The hardness of the Cu and Mo layers in different zones with different rolling processes is shown in Fig. 12. The hardness of the Mo layer is significantly higher than that of the Cu layer. As the rolling reduction increased, the hardness of the Cu layer increased gradually. This can be attributed to the increased LAGBs and the decreased grains size with increasing rolling reductions. For certain rolling reduction, there is no obvious difference in the hardness of the Cu layer in different zones. Because the rolling temperature far exceeds the recrystallization temperature of Cu, the Cu layer has low deformation resistance. The shear force from the Mo layer and roller has little effect on the hardness of the Cu layer. The hardness of Mo layer increases obviously with increasing rolling

reduction. The deformation of the Mo layer gradually increases as the total rolling reduction increases and the improvement in hardness is a result of work hardening [42]. The hardness of the Mo layer of the near-interface zone is higher than that of the middle zone, which is caused by the shear stress from the Cu layer [43].

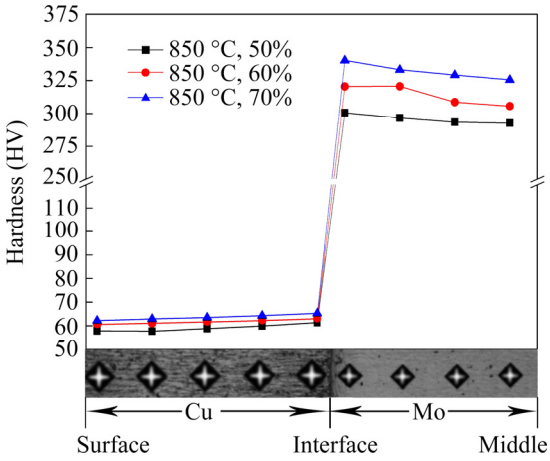

Fig. 12 Hardness of Cu and Mo layers in different zones with different rolling processes

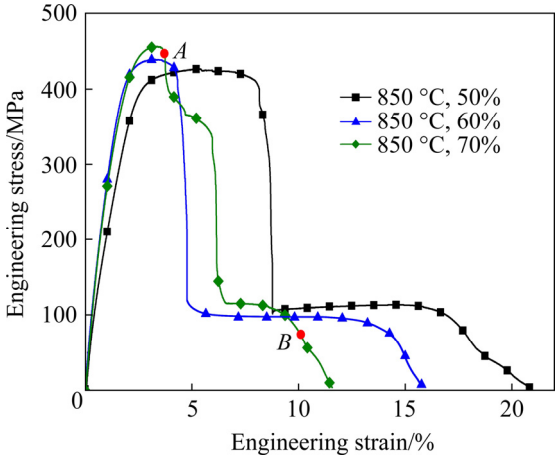

Fig. 13 Tensile curves of Cu/Mo/Cu clad sheets under different conditions

Figure 13 shows the tensile curves of Cu/Mo/Cu clad sheets with different rolling reductions. It was obvious that the elastic modulus of the rolling reduction of 60% is almost the same as 70% reduction but higher than 50% reduction. The elastic modulus of clad sheets corresponds to the rule of mixture [44]: $E_{Cu/Mo/Cu}=E_{Cu}\varphi_{Cu}+E_{Mo}\varphi_{Mo}$, where $E_{Cu/Mo/Cu}$ is the elastic modulus of Cu/Mo/Cu clad sheets, E_{Cu} and φ_{Cu} are the elastic modulus and volume fraction of Cu respectively, and E_{Mo} and φ_{Mo} are the elastic modulus and volume fraction of Mo, respectively. The elastic moduli of 50%, 60% and 70% reductions are 178.767, 187.875 and 186.627 GPa, respectively. In addition, the strength of Cu/Mo/Cu clad sheets is increased with the increase of reduction. This can be explained that Mo experiences larger plastic deformation and work hardening plays an important role in enhancing the strength [45]. The strength of the clad sheets is determined by the Mo layer and the elongation is determined by the Cu layer. The total elongation was decreased with the increasing reduction. It depends on the recrystallization degree of the Cu layer. As shown in Figs. 7 and 8, the grains almost completely recrystallize when the rolling reduction is 50%, and the clad sheets have higher elongation. The LAGBs of the Cu layer gradually increase, as presented in Fig. 7. When subjected to an external force, these local deformation zones easily occur to work hardening, resulting in plasticity reduction. Additionally, according to the above, a larger rolling reduction contributes to the well interface bonding which has an adverse effect on the ductility [46,47].

Figure 14 demonstrates the fracture morphologies of the clad sheets under 70% reduction. All tensile curves show a “drop in” phenomenon in Fig. 13, which may be attributed to premature interface delamination, such as Fig. 14(a), causing a loss in the load support capabilities of the Cu/Mo/Cu clad sheets. Figures 14(a) and (b) show the RD−ND plane fracture morphologies at different stages of the tensile curve, which correspond to points *A* and *B*, respectively. The outer Cu has undergone a large plastic deformation, and there is an obvious necking phenomenon, as shown in the rectangular frames of Fig. 14(b). The TD−ND plane fracture morphologies of the outer and near-interface Cu layers are presented in Figs. 14(c) and (d), respectively. It is obvious that the outer Cu layer presents shallow parabolic dimples at greater depths, while the region near the interface is relatively smooth and shows a fibrous shape and it is cleavage fracture. It can be explained that for the Cu layer near the interface, due to the constraint of the Mo layer, there is no obvious plastic deformation or necking. The TD−ND plane fracture morphology of Mo is shown in Fig. 14(e). The Mo layer shows obvious delamination fracture. During the rolling process, the grains of the Mo layer were severely deformed and elongated. A lot

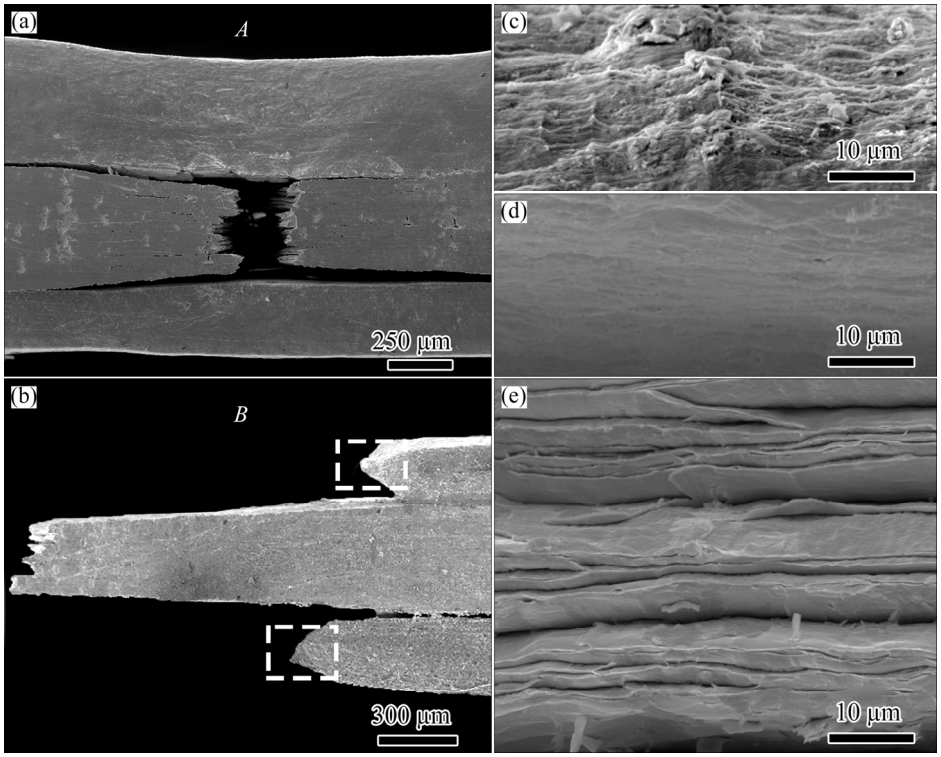

Fig. 14 Fracture morphologies of clad sheets of 70% reduction: RD−ND plane fracture morphologies (a, b) of points *A* and *B* in Fig. 13, respectively, TD−ND plane fracture morphologies of outer (c) and near-interface (d) Cu layers, and TD−ND plane fracture morphology (e) of Mo layer

of defects converge at the grain boundaries to form microcracks. During the tensile process, the microcracks gather and extend along the grain boundaries and consequently lead to the delamination of Mo. A similar rupture behavior was also reported by previous researchers [48].

3.6 Thermal expansion property and establishment of CTE prediction model

In general, an excellent combination interface can achieve the transmission of force [49]. According to the above result, a larger rolling reduction contributes to the formation of a sound interface. Therefore, the three specimens with 70% reduction at 850, 900 and 950 °C were analyzed and the corresponding volume fractions of Mo were 35.1%, 32.9% and 29.3%, respectively. In order to exclude the effect of internal stress in the rolled clad sheets, the three specimens were annealed at 400 °C for 1 h. The linear thermal expansion curves of different rolling temperatures of clad sheets are shown in Fig. 15. The linear thermal expansion value can be defined as $\Delta L/L_0$, and the CTE (α) is defined as

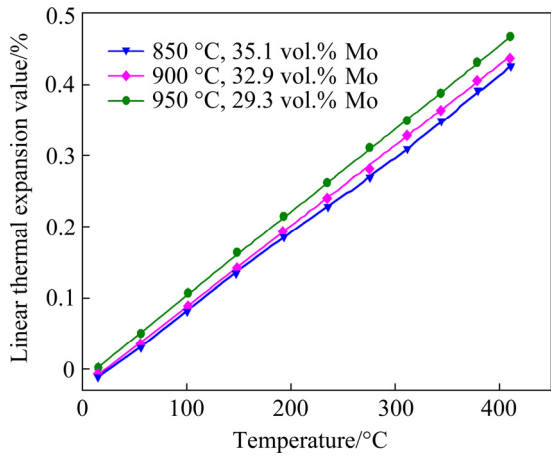

Fig. 15 Linear thermal expansion curves of annealed Cu/Mo/Cu clad sheets fabricated at different rolling temperatures with reduction of 70% corresponding to different volume fractions of Mo

$$\alpha = \frac{1}{\Delta T} \cdot \frac{\Delta L}{L_0} \tag{1}$$

where L_0 is the original length of the sample, ΔL is the change in the length over a temperature interval ΔT, and the unit of CTE (α) is K^{-1}.

According to the principle of Formula (1), the experimental CTE values of Cu/Mo/Cu clad sheets

were measured and the results are 10.9×10^{-6}, 11.0×10^{-6} and $11.5\times10^{-6}\,K^{-1}$ corresponding to 35.1%, 32.9% and 29.3% volume fractions of Mo, respectively. It can be found that the CTE gradually decreases with the increase of volume fraction of Mo.

Finite element simulation can provide visual deformation and stress distributions. To prove the accuracy of the simulation method, it is necessary to compare the simulated and experimental CTE values. Figure 16 shows the experimental and simulated results of different volume fractions of Mo. Here, the CTE values are determined to the outermost end face of the clad sheets during the simulation process.

As shown in Fig. 16, the change trend of simulated CTE (α_s) is in agreement with the experimental CTE (α_e), but the values of α_s are slightly smaller than α_e. The error of CTE (ε_α) can be defined as

$$\varepsilon_\alpha = \frac{\alpha_e - \alpha_s}{\alpha_e} \times 100\% \quad (2)$$

Based on Formula (2), the three errors of CTE (ε_α) are 2.43%, 2.27% and 3.12% corresponding to 29.3%, 32.9% and 35.1% volume fractions of Mo, respectively. It can be inferred that the simulation method is effective and can be used to analyze the deformation and stress distribution in the process of thermal expansion. Simultaneously, finite element simulation can be used to calculate the CTE with other volume fractions of Mo.

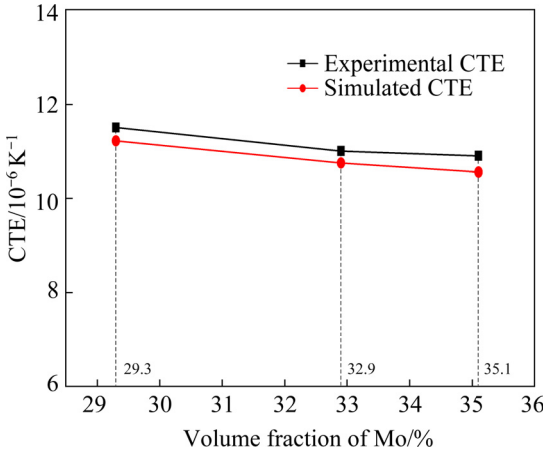

Fig. 16 Results of experimental and simulated CTE with different volume fractions of Mo

Stress distribution reflects the interaction of Cu and Mo layers under the effect of thermal loading. Figure 17 illustrates the deformation and the cloud map of the equivalent stress and strain

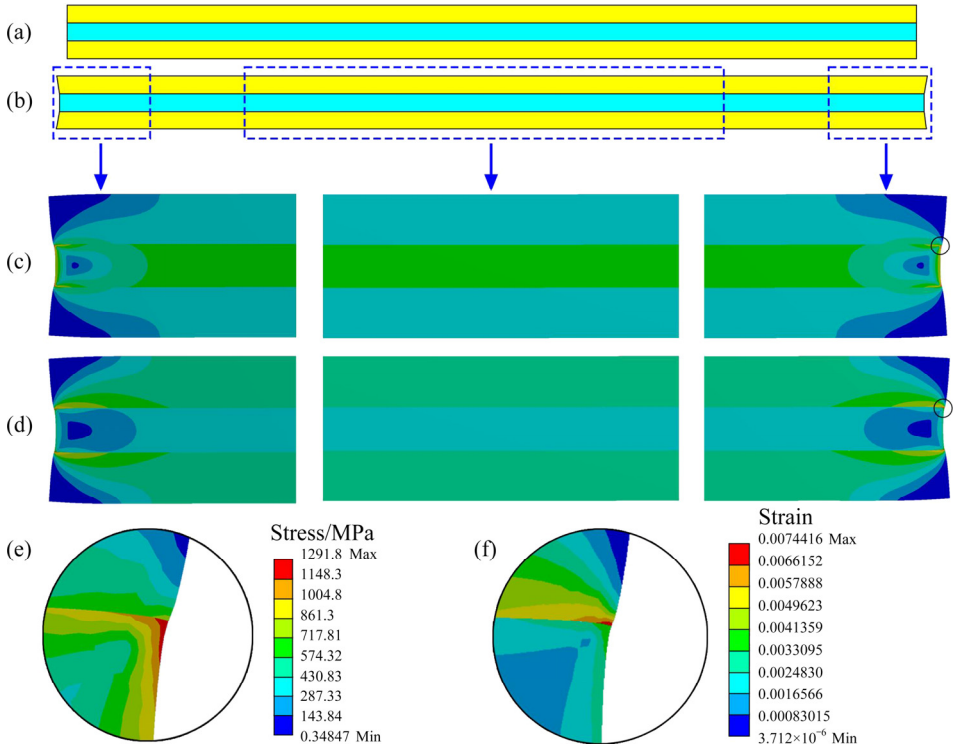

Fig. 17 Schematic diagrams of initial (a) and thermal-expansion (b) Cu/Mo/Cu clad sheets with volume fraction of Mo 32.9%, equivalent stress (c) and equivalent strain (d) distributions in (b), respectively, and enlargements of circular areas (e, f) in (c) and (d), respectively

distributions when the volume fraction of Mo is 32.9%. The equivalent stress and strain cloud diagrams show a centrosymmetric distribution. Notably, the terminal face of the clad sheets is sunken inward. When the Cu/Mo/Cu clad sheets get a thermal load, it will inevitably expand. Due to the difference in CTE, the deformation of Cu is larger than Mo. The Cu layer will pull the Mo layer to the outside and the Mo layer will prevent the Cu layer to the outside. The near-interface side of the Cu layer is constrained by the interface, but the part away from the interface can expand freely and then form the deformation in Fig. 17(b). At the same time, it is obvious that the homogeneous stress and strain are distributed in most areas of the clad sheets, indicating that most area of Cu and Mo layers can achieve homogeneous deformation under the effect of thermal loading. Concentrated stress and strain only appear in the end face on two sides, as shown in Figs. 17(c) and (d). The maximum stress can reach 1291.8 MPa, as presented by the circular shape in Figs. 17(e) and (f), so it can be speculated that the end of the interface is a place where cracks easily appear. This result is similar to the thermal stress distribution of PC/Cu/PC by laser transmission welding [50].

The Cu/Mo/Cu clad sheets can be abstracted as a fiber-reinforced composite material, with the Mo layer as the matrix and the Cu layer as the reinforcement. It can be tried to use the Schapery's model to predict the CTE values [51,52]. At the same time, the model considers the interaction between each component material. The CTE between single metal and clad sheets satisfies the following formula:

$$\alpha_{\mathrm{CMC}}=\frac{2\alpha_{\mathrm{Cu}}E_{\mathrm{Cu}}H_{\mathrm{Cu}}+\alpha_{\mathrm{Mo}}E_{\mathrm{Mo}}H_{\mathrm{Mo}}}{2E_{\mathrm{Cu}}H_{\mathrm{Cu}}+E_{\mathrm{Mo}}H_{\mathrm{Mo}}} \tag{3}$$

where E represents the elastic modulus, and H represents the thickness. The subscripts 'CMC' represents the Cu/Mo/Cu. We can regard the result calculated by Formula (3) as the theoretical CTE of Cu/Mo/Cu clad sheets.

Formula (3) can be rewritten as

$$\alpha_{\mathrm{CMC}}=\frac{2\alpha_{\mathrm{Cu}}E_{\mathrm{Cu}}i+\alpha_{\mathrm{Mo}}E_{\mathrm{Mo}}}{2E_{\mathrm{Cu}}i+E_{\mathrm{Mo}}} \tag{4}$$

where parameter i represents the layer thickness ratio ($H_{\mathrm{Cu}}/H_{\mathrm{Mo}}$). It can be found that the CTE of the Cu/Mo/Cu clad sheets is only related to α_{Cu}, α_{Mo}, E_{Cu}, E_{Mo} and i, and is unrelated to the length of the clad sheets and the thickness of two component metals.

Figure 18 presents that the simulated CTE values of the clad sheets are larger than the theoretical CTE. The theoretical calculation model ignores the effect of the total thickness of the clad sheets on the CTE and considers that the end face of the clad sheets is flat after the thermal expansion [53]. However, according to the simulation results, the end face of the clad sheets was sunken inward. The elongation of the free end of the Cu layer will have an effect on the CTE, and the simulation value will be larger than the theoretical calculation result. The theoretical calculation model can be modified to make it close to the simulated result, so that the CTE can be predicted directly through theoretical calculation in practical applications. It is assumed that the CTE obtained by theoretical calculation and the corrected CTE satisfy the following relationship:

$$\alpha_j'=k\alpha_j \tag{5}$$

where α_j is the CTE obtained through the theoretical calculation, α_j' is the corrected CTE, and k is the

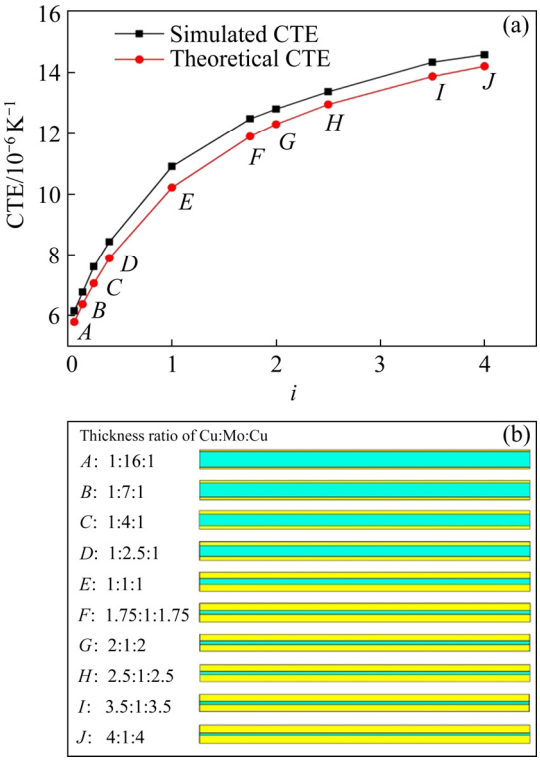

Fig. 18 Simulated and theoretical CTE of Cu/Mo/Cu clad sheets (a), and cross-section schematic diagram of sheets with different thickness ratios (b)

correction factor. Then, k is a coefficient related to the layer thickness ratio. For this reason, a scatter plot of the k value and the layer thickness ratio i can be established to perform curve fitting, and the linear fitting is preferred.

The linear fitting diagram of the k value and the layer thickness ratio i is shown in Fig. 19. Based on the above, the following formula can be obtained:

$$\alpha_j' = (-0.01i + 1.0653)\alpha_j \quad (6)$$

The corrected theoretical CTE is compared with the simulated CTE, as shown in Fig. 20. The revised theoretical calculation results and the simulation results overlap very well. Therefore, the corrected theoretical model can be used to predict the thermal expansion coefficient of the clad sheets. The final prediction model is:

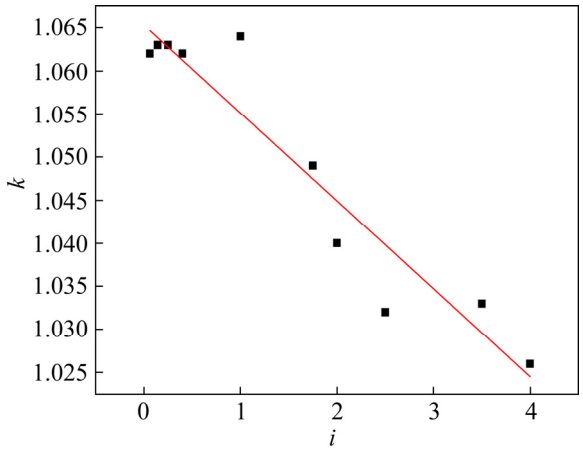

Fig. 19 Linear fitting result of correction factor and layer thickness ratio

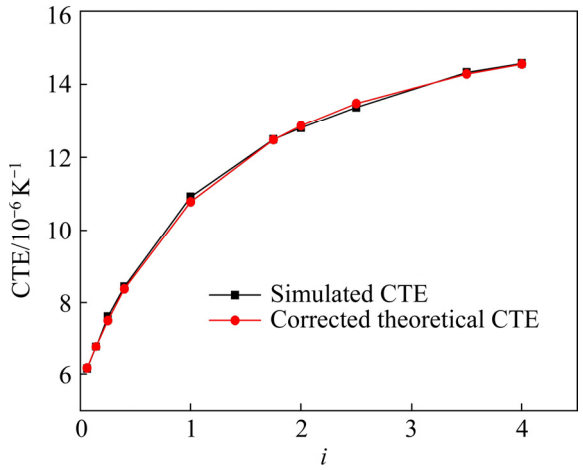

Fig. 20 Simulated and corrected theoretical CTE of clad sheets

$$\alpha_{CMC} = (1.0653 - 0.01i) \cdot \frac{2\alpha_{Cu}E_{Cu}i + \alpha_{Mo}E_{Mo}}{2E_{Cu}i + E_{Mo}} \quad (7)$$

Based on the above, the corrected theoretical model can predict the CTE of clad sheets well, which can provide guidance for actual production. In the current research, the prediction of CTE is mostly focused on composite materials. WU and DRZAL [51] investigated the effect of graphene nanoplatelets on the CTE of polyetherimide composite and found that the Schapery's lower limit model fit the experimental CTE very well. KUMAR et al [54] studied the CTE of carbon nanotube-reinforced silver composites using the rule of mixture and Schapery's model. GAO et al [55] suggested that a modified Kerner model was fitted to express the temperature dependence of $MoSi_2$−RSiC composites. Different from composite materials, the deformation of each part of the clad sheets is inhomogeneous after heating. Therefore, in this work, the existing model of the CTE of composite material was corrected based on the results of finite element simulation.

4 Conclusions

(1) The straight Cu/Mo interface changed into a wavy morphology with increased rolling reduction and the larger reduction contributed to the sound interface bonding. The increased rolling reduction and temperature promoted the collaborative deformation of Cu and Mo.

(2) The microstructure and texture through the thickness of Cu and Mo layers were inhomogeneous due to the shear effect between the roller and sheet surface as well as the uncoordinated deformation between two component metals.

(3) The strength of clad sheets was increased with the increase of rolling reduction, but the change trend of elongation was opposite. The clad sheets underwent premature interface delamination during tensile testing. The CTE of Cu/Mo/Cu clad sheets gradually decreased with the increase of volume fraction of Mo.

(4) Finite element simulation presented the thermal expansion behavior and predicted the CTE of Cu/Mo/Cu clad sheets. The terminal face of the clad sheets was sunken inward under the thermal load due to the difference in the thermal expansion properties of two metals. The following theoretical calculation model can be set up to predict the CTE

of Cu/Mo/Cu clad sheets directly:

$$\alpha_{CMC}=(1.0653-0.01i)\cdot\frac{2\alpha_{Cu}E_{Cu}i+\alpha_{Mo}E_{Mo}}{2E_{Cu}i+E_{Mo}}$$

Acknowledgments

The authors are grateful for the financial supports from the National Natural Science Foundation of China (No. 51421001), the Fundamental Research Funds for the Central Universities, China (Nos. 2019CDQYCL001, 2019CDCGCL204, 2020CDJDPT001), and the Research Project of State Key Laboratory of Vehicle NVH and Safety Technology, China (No. NVHSKL-201706).

References

[1] LIU H S, ZHANG B, ZHANG G P. Enhanced toughness and fatigue strength of cold roll bonded Cu/Cu laminated composites with mechanical contrast [J]. Scripta Materialia, 2011, 65: 891−894.

[2] ZHANG G F, YANG X H, ZHU D H, ZHANG L J. Cladding thick Al plate onto strong steel substrate using a novel process of multilayer-friction stir brazing (ML-FSB) [J]. Materials & Design, 2020, 185: 108232.

[3] DU J L, HUANG Y, XIAO C, LIU Y C. Building metallurgical bonding interfaces in an immiscible Mo/Cu system by irradiation damage alloying (IDA) [J]. Journal of Materials Science & Technology, 2018, 34: 689−694.

[4] WANG D Z, CHEN D D, YANG Y H, SUN A K. Interface of Mo−Cu laminated composites by solid-state bonding [J]. International Journal of Refractory Metals and Hard Materials, 2015, 51: 239−242.

[5] YAO J T, LI C J, LI Y, CHEN B, HUO H B. Relationships between the properties and microstructure of Mo−Cu composites prepared by infiltrating copper into flame-sprayed porous Mo skeleton [J], Materials & Design, 2015, 88: 774−780.

[6] KANG S, NANDI R, SIM J K, JO J Y, CHATTERJEE U, LEE C R. Characteristics of an oxide/metal/oxide transparent conducting electrode fabricated with an intermediate Cu−Mo metal composite layer for application in efficient CIGS solar cell [J]. RSC Adv, 2017, 7: 48113−48119.

[7] SINGH M, ASTHANA R. Characterization of brazed joints of C−C composite to Cu-clad-molybdenum [J]. Composites Science and Technology, 2008, 68: 3010−3019.

[8] WACHOWSKI M, GLOC M, ŚLĘZAK T, PŁOCIŃSKI T, KURZYDŁOWSKI K J. The effect of heat treatment on the microstructure and properties of explosively welded titanium−steel plates [J]. Journal of Materials Engineering and Performance, 2017, 26: 945−954.

[9] SEISS M, MROTZEK T, DREER N, KNABL W. Molybdenum−copper-composites for the advanced thermal management of modern electronics [J]. Materials Science Forum, 2015, 825: 297−304.

[10] ZHANG J, SHEN Q, LUO G Q, LI M J, ZHANG L M. Microstructure and bonding strength of diffusion welding of Mo/Cu joints with Ni interlayer [J]. Materials & Design, 2012, 39: 81−86.

[11] YANG Y H, LIN G Y, WANG X Y, CHEN D D, SUN A K, WANG D Z. Fabrication of Mo−Cu composites by a diffusion-rolling procedure [J]. International Journal of Refractory Metals and Hard Materials, 2014, 43: 121−124.

[12] KIM I K, HONG S I. Mechanochemical joining in cold roll-cladding of tri-layered Cu/Al/Cu composite and the interface cracking behavior [J]. Materials & Design, 2014, 57: 625−631.

[13] RAHMATABADI D, MOHAMMADI B, HASHEMI R, SHOJAEE T. An experimental study of fracture toughness for nano/ultrafine grained Al5052/Cu multilayered composite processed by accumulative roll bonding [J]. Journal of Manufacturing Science and Engineering, 2018, 140: 101001.

[14] ZHANG X P, CASTAGNE S, YANG T H, GU C F, WANG J T. Entrance analysis of 7075 Al/Mg−Gd−Y−Zr/7075 Al laminated composite prepared by hot rolling and its mechanical properties [J]. Materials & Design, 2011, 32: 1152−1158.

[15] ZHANG X B, YU Y B, LIU B, ZHAO Y C, REN J Q, YAN Y J, CAO R, CHEN J H. In-situ investigation of deformation behavior and fracture mechanism of laminated Al/Ti composites fabricated by hot rolling [J]. Journal of Alloys and Compounds, 2019, 783: 55−65.

[16] NIE H H, HAO X W, CHEN H S, KANG X P, WANG T L, MI Y J, LIANG W. Effect of twins and dynamic recrystallization on the microstructures and mechanical properties of Ti/Al/Mg laminates [J]. Materials & Design, 2019, 181: 107948.

[17] RAHMATABADI D, TAYYEBI M, SHEIKHI A, HASHEMI R. Fracture toughness investigation of Al1050/Cu/MgAZ31ZB multi-layered composite produced by accumulative roll bonding process [J]. Materials Science and Engineering A, 2018, 734: 427−436.

[18] RAHMATABADI D, TAYYEBI M, HASHEMI R, FARAJI G. Microstructure and mechanical properties of Al/Cu/Mg laminated composite sheets produced by the ARB process [J]. International Journal of Minerals, Metallurgy and Materials, 2018, 25: 564−572.

[19] DU J J, ZHANG X, LIU B X, DONG Y.C, FENG J H, CHEN C X, YIN F X. Interface strengthening and fracture behavior of multilayer TWIP/TRIP steel [J]. Materials Chemistry and Physics, 2019, 223: 114−121.

[20] ZHANG B Y, LIU B X, HE J N, FANG W, ZHANG F Y, ZHANG X, CHEN C X, YIN F X. Microstructure and mechanical properties of SUS304/Q235 multilayer steels fabricated by roll bonding and annealing [J]. Materials Science and Engineering A, 2019, 740/741: 92−107.

[21] KIM H S, On the rule of mixtures for the hardness of particle reinforced composites [J]. Materials Science and Engineering A, 2000, 289: 30−33.

[22] CUI W, LI S Q, YAN J C, ZHANG X. Microstructure and mechanical performance of composite joints of sapphire by ultrasonic-assisted brazing [J]. Journal of Materials Processing Technology, 2018, 257: 1−6.

[23] WANG K, JIANG T, HUANG Z L, XUE H S, YANG D Z, ZHU Z Z. Mechanical and thermal expansion properties of SiC_P/ZAlSi9Mg composites produced by centrifugal casting [J]. Journal of Wuhan University of Technology (Materials Science Edition), 2016, 31: 197−203.

[24] YOUNG B A, WEI Z H, RUBALCAVA-CRUZ J R, FALZONE G, KUMAR A, NEITHALATH N, SANT G, PILON L. A general method for retrieving thermal deformation properties of microencapsulated phase change materials or other particulate inclusions in cementitious composites [J]. Materials & Design, 2017, 126: 259−267.

[25] MO T Q, CHEN J, CHEN Z J, HE W J, LIU Q. Microstructure evolution during roll bonding and growth of interfacial intermetallic compounds in Al/Ti/Al laminated metal composites [J]. JOM, 2019, 71: 4769−4777.

[26] LI B X, HE W J, CHEN Z J, HUANG H T, PENG L, LI J, LIU Q. Evolution of interface and collaborative deformation between Ti and steel during hot roll bonding [J]. Materials Characterization, 2020, 164: 110354.

[27] LI X B, ZU G Y, WANG P. Microstructural development and its effects on mechanical properties of Al/Cu laminated composite [J]. Transactions of Nonferrous Metals Society of China, 2015, 25: 36−45.

[28] MA M, HUO P, LIU W C, WANG G J, WANG D M. Microstructure and mechanical properties of Al/Ti/Al laminated composites prepared by roll bonding [J]. Materials Science and Engineering A, 2015, 636: 301−310.

[29] ZHANG J T, LIN J B, WANG Q Q, DU X L, WANG Y H. Recrystallization behaviour during annealing of cold-rolled Cu−5Fe−2Sn alloy [J]. Materials Science and Technology, 2020, 36: 1162−1168.

[30] ABBASI M, DEHGHANI M, GUIM H U, KIM D I. Investigation of Fe-rich fragments in aluminum−steel friction stir welds via simultaneous Transmission Kikuchi Diffraction and EDS [J]. Acta Materialia, 2016, 117: 262−269.

[31] WANG C P, LI F G, LI Q H, WANG L. Numerical and experimental studies of pure copper processed by a new severe plastic deformation method [J]. Materials Science and Engineering A, 2012, 548: 19−26.

[32] SHIN J H, PARK J S, BAE D H. Fabrication of supersaturated Cu−Sn alloy sheets and their antibacterial properties [J]. Metals and Materials International, 2011, 17(3): 441−444.

[33] PAN H C, QIN G W, HUANG Y M, REN Y P, SHA X C, HAN X D, LIU Z Q, LI C F, WU X L, CHEN H W, HE C, CHAI L J, WANG Y Z, NIE J F. Development of low-alloyed and rare-earth-free magnesium alloys having ultra-high strength [J]. Acta Materialia, 2018, 149: 350−363.

[34] FIELD D P, BRADFORD L T, NOWELL M M, LILLO T M. The role of annealing twins during recrystallization of Cu [J]. Acta Materialia, 2007, 55: 4233−4241.

[35] EBRAHIMI G R, MOMENI A, EZATPOUR H R, JAHAZI M, BOCHER P. Dynamic recrystallization in Monel400 Ni−Cu alloy: Mechanism and role of twinning [J]. Materials Science and Engineering A, 2019, 744: 376−385.

[36] XUE K M, ZHOU Y F, TIAN W C, LI P. Texture evolution and deformation-induced amorphization in high pressure torsion of W [J]. Materials Today Communications, 2020, 24: 101178.

[37] WANG S, WU Z H, XIE M Y, SI D H, LI L Y, CHEN C, ZHANG Z, WU Y C. The effect of tungsten content on the rolling texture and microstructure of Ta−W alloys [J]. Materials Characterization, 2020, 159: 110067.

[38] DENG C, LIU S F, JI J L, HAO X B, ZHANG Z Q, LIU Q. Texture evolution of high purity tantalum under different rolling paths [J]. Journal of Materials Processing Technology, 2014, 214: 462−469.

[39] ZHU J L, LIU S F, LIU Y H, LIN N, YANG S, DENG C, LIU Q. Deformation and annealing behavior in the ‘interaction zone’ of cold-rolled tantalum sheets [J]. Vacuum, 2019, 164: 105−113.

[40] DHINWAL S S, TOTH L S, HODGSON P D, HALDAR A. Effects of processing conditions on texture and microstructure evolution in extra-low carbon steel during multi-pass asymmetric rolling [J]. Materials, 2018, 11: 1327.

[41] YOU Shi-wu. Investigation of textures in cold-rolled pure Mo plates [J]. Physical Testing and Chemical Analysis (Part A): Physical Testing, 2000, 36: 342−344.

[42] WANG D Z, JI Y X, WU Z Z. Effects of cross rolling on texture, mechanical properties and anisotropy of pure Mo plates [J]. Transactions of Nonferrous Metals Society of China, 2020, 30: 2170−2176.

[43] MISRA A, ZHANG X, HAMMON D, HOAGLAND R G. Work hardening in rolled nanolayered metallic composites [J]. Acta Materialia, 2005, 53: 221−226.

[44] SEOK M Y, LEE J A, LEE D H, RAMAMURTY U, NAMBU S, KOSEKI T, JANG J. Decoupling the contributions of constituent layers to the strength and ductility of a multi-layered steel [J]. Acta Materialia, 2016, 121: 164−172.

[45] MO T Q, CHEN Z J, LI B X, WANG P J, LIU Q. Tailoring of interface structure and mechanical properties in ARBed 1100/7075 laminated composites by cold rolling [J]. Materials Science and Engineering A, 2019, 755: 97−105.

[46] MASHHADI A, ATRIAN A, GHALANDARI L. Mechanical and microstructural investigation of Zn/Sn multilayered composites fabricated by accumulative roll bonding (ARB) process [J]. Journal of Alloys and Compounds, 2017, 727: 1314−1323.

[47] YOUSEFI MEHR V, TOROGHINEJAD M R, REZAEIAN A. Mechanical properties and microstructure evolutions of multilayered Al−Cu composites produced by accumulative roll bonding process and subsequent annealing [J]. Materials Science and Engineering A, 2014, 601: 40−47.

[48] KREIML P, RAUSCH M, TERZIYSKA V L, KÖSTENBAUER H, WINKLER J, MITTERER C, CORDILL M J. Balancing the electro-mechanical and interfacial performance of Mo-based alloy films [J]. Materialia, 2020, 12: 100774.

[49] LI Y, WONG C P. Recent advances of conductive adhesives as a lead-free alternative in electronic packaging: Materials, processing, reliability and applications [J]. Materials Science and Engineering R, 2006, 51: 1−35.

[50] WANG C Y, YU X D, JIANG M H, XING Z W, WANG C D. Numerical and experimental investigation into the evolution and distribution of residual stress in laser transmission welding of PC/Cu/PC [J]. Optics & Laser Technology, 2021, 136: 106786.

[51] WU H, DRZAL L T. Effect of graphene nanoplatelets on coefficient of thermal expansion of polyetherimide composite [J]. Materials Chemistry and Physics, 2014, 146: 26−36.
[52] ZHANG Y, LI J W, ZHAO L L, ZHANG H L, WANG X T. Effect of metalloid silicon addition on densification, microstructure and thermal–physical properties of Al/diamond composites consolidated by spark plasma sintering [J]. Materials & Design, 2014, 63: 838−847.
[53] MAKARIAN K, SANTHANAM S. Micromechanical modeling of thermo-mechanical properties of high volume fraction particle-reinforced refractory composites using 3D finite element analysis [J]. Ceramics International, 2020, 46: 4381−4393.
[54] KUMAR D, NAIN S, KUMAR R, PAL H. Thermal expansion studies of carbon nanotube-reinforced silver nanocomposite [J]. Zeitschrift für Naturforschung A, 2015, 70: 63–67.
[55] GAO P Z, XU M Y, YUAN Z, CHENG L, LIANG J J, XIAO H N, CHEN R H. Temperature dependence of the mechanical and thermal expansion behaviors of $MoSi_2$−RSiC composites with a three-dimensionally (3D) interpenetrated network structure [J]. Journal of Alloys and Compounds, 2018, 731: 1103−1111.

热轧制备 Cu/Mo/Cu 复合板的组织演变、力学性能与热膨胀系数的调控

刘江江，陈泽军，周湛淞，莫太骞，王鹏举，何维均

重庆大学 材料科学与工程学院 教育部轻合金材料国际合作联合实验室，重庆 400044

摘 要：系统研究热轧制备 Cu/Mo/Cu 复合板的组织演变规律和力学性能，成功建立 Cu/Mo/Cu 复合板热膨胀系数(CTE)的理论预测模型。结果表明，随着轧制压下量和轧制温度的上升，Cu 和 Mo 层的变形逐渐趋于一致，在较大的轧制压下量下实现良好的界面结合。Cu 和 Mo 层沿厚度方向的显微组织和织构是不均匀的，这种现象可归因于轧辊与板材表面的摩擦以及 Cu 和 Mo 之间的不协调变形。复合板的抗拉强度随着轧制率的增加而增加，伸长率逐渐降低。 Cu/Mo/Cu 复合板的 CTE 与 Mo 的体积分数密切相关。有限元方法可以模拟热膨胀过程中的变形和应力分布，模拟结果表明复合板的端面向内凹陷。

关键词：Cu/Mo/Cu 复合板；轧制复合；协同变形；力学性能；热膨胀系数；预测模型

(Edited by Xiang-qun LI)